# Experimental study on effects of gas flow rate on soot characteristics in diffusion flames coupled with plasma

Dandan Qi[1,2], Mingxiao Chen[1,2], Xin Tu[3], Dong Liu[1,2,*]

[1] *MIIT Key Laboratory of Thermal Control of Electronic Equipment, School of Energy and Power Engineering, Nanjing University of Science and Technology, Nanjing 210094, People's Republic of China.*

[2] *Advanced Combustion Laboratory, School of Energy and Power Engineering, Nanjing University of Science and Technology, Nanjing 210094, People's Republic of China.*

[3] *Department of Electrical Engineering and Electronics, University of Liverpool, Liverpool L69 3GJ, UK*

[*] Corresponding author. E-mail: dongliu@njust.edu.cn (Dong Liu)

**Abstract**

This paper examined the evolution of morphology and nanostructure of soot particles from the plasma-flame interaction for various gas flow rates. The current study used both optical diagnostic and sampling methods to explore the soot production and combustion characteristics. Soot particles were characterized at the same positions downstream from the flame zone by thermophoretic sampling and transmission electron microscopy. Moreover, X-ray diffraction analysis, and thermogravimetric analysis were performed to study the nanostructure and oxidation reactivity of soot. A reduction in soot concentration was found with the plasma addition, which illustrated an inhibition effect of plasma on soot emission. The increased gas flow rate promoted soot concentration since a growing number of carbons participated in the combustion process. Depending on the gas flow rate (carbon content) variation and plasma activation, either liquid-like soot material with irregularly shaped protrusions or chain-like structure, or a mixture of both, were generated from the diffusion flames. The soot produced by plasma-flame interaction also demonstrated a high correlation between nanostructure and reactivity. The soot from lower carbon content with plasma activation had a shorter fringe length and larger fringe tortuosity related to higher oxidation reactivity. On the contrary, soot from the highest carbon content without plasma-flame interaction exhibited prevalent fullerene-like nanostructures with evident large or small shells and also had a higher carbonization degree resulting in lower oxidation reactivity.

***Keywords:*** Soot characteristics, Gas flow rate, Plasma, Diffusion flames

## 1. Introduction

Combustion generates a range of air pollutants, including soot, nitrogen oxides ($NO_x$), sulfur oxides ($SO_x$), and unburned hydrocarbons. Soot emissions are known to have adverse effects on human health and the environment [1-3]. Fine particulate matter (PM), less than 2.5 μm, and ultrafine PM, less than 0.1 μm, can penetrate deep into the lungs [4]. Plasma-assisted combustion (PAC) has emerged as a potent technology to affect combustion processes such as improved combustion efficiency [5-7], reduced pollutant emissions [8-11], and shorten ignition delays [12-15]. In the case of soot formation, small changes in the plasma parameters or combustion conditions can alter the characteristics of the resulting soot particles radically under the interaction of plasma and flame.

Compared to thermal plasma, non-thermal plasma (NTP) has higher electron temperature and is more kinetically active due to the rapid production of active radicals and excited species via electron impact dissociation, excitation, and subsequent energy relaxation. Recently, the combination of NTP and combustion has become an emerging alternative for the control of pollutants emission in combustion [16, 17]. Plasma-flame interaction has many advantages over other methods such as adding compounds and catalysts. As a continuous process, plasma-flame interaction is more scalable than the follow-up treatment of pollutants. Plasma activation uses common flames as objects and does not require the use of strong chemicals, which are often costly and can introduce undesirable phases, and contamination [18]. Varella et al. [19] evaluated the effect of PAC on pollutant emissions from a premixed flame.

The generation of free radicals and excited state substances increased, hastening the oxidation of CO and methane burning. The plasma could affect the soot formation process and combustion characteristics [8, 9, 20, 21]. Cha et al. reported the formation of soot but the properties of this material were not analyzed [9]. Soot oxidation in a plasma-catalytic reactor showed that the weak component of the particle floc structure broke first during oxidation to form a chain structure [22]. Other studies include the simultaneous treatment of soot and $NO_x$ utilizing catalysis combined with the non-thermal plasma [23]. It was shown that the transition of the soot formation strongly depends on the carbon concentration in the gas phase as determined by the reactant concentration through plasma [24, 25]. Besides, in gas discharge, the variation of gas flow rate is also an important variable to change the characteristics of plasma. It remains unclear, however, what role gas flow rate plays in soot formation during plasma-flame interaction. Temperatures and electron density decreased with the gas flow in argon surface-wave discharges sustained at atmospheric pressure [26]. The authors suggested that was due to the reduced residence time of heavy particles and electrons. However, it is yet unknown how the flow rate affects temperature and soot concentration in the interaction between plasma and flame.

Considering the remarkable performance of plasma in reducing soot emission [9], the aforementioned studies mainly focused on the variation of overall flame shapes or the kinetic analysis. In our previous, we investigated the detailed influences of oxygen in the plasma-flame interaction on soot emissions and characteristics [8]. Soot nanostructure and oxidation reactivity research contribute to a better understanding of

the soot generation process and the development of efficient soot reduction devices. According to the previous research [27,28], the gas flow rate both affected soot formation and combustion characteristic. In this paper, we further delved into the study of how flow rate affected the formation of soot particles in plasma-flame interactions. We aimed to elucidate how the nanoparticles evolved under the plasma-flame interaction by investigating three flow rates that led to the differences in soot properties.

In the present work, we systematically investigated the effect of gas flow rate on the characteristic of soot particles in plasma-flame interaction. We studied the effect of plasma activation on the flame at different gas flow rates at the same carbon-to-oxygen (C/O) ratio. Crucially, we compared the characteristics of soot particles with varying gas flow rates under plasma-free conditions. This comparison allowed us to elucidate the role of plasmas in the combustion. The temperature and soot concentration were performed by the situ optical diagnostics.

## 2. Experimental set-up and characterization

In this study, the experimental system consisted of: (i) a dielectric-barrier discharge (DBD)-plasma system, (ii) a quartz burner system, (iii) a thermophoretic sampling device, (iv) a quartz plate sampling system with circulating water, and (v) an optical diagnostic system. The quartz burner used here was the same as our previous work [8]. The burner featured an inner fuel nozzle made of a quartz tube as well as a coaxial outer tube, as illustrated schematically in Fig. 1. The coflow oxidant was delivered through the outer tube. The fuel was ethylene (>99.95%), and the mixture of

nitrogen and oxygen was used as an oxidizer. Mass-flow controllers (CS200A) were used for flow rate control with 98% accuracy. The gaseous reactants were fed to the reactor through the reactor's bottom nozzle. The sample rate of the oscilloscope is 2 GS/s. It was insulated from the outside environment since the combustion took place inside the burner. A DBD reactor, an electrical parameter monitoring system, and a power supply comprised the nonthermal plasma generation system. Plasma was generated in the flame's root zone, where substances in the flame interacted with the plasma and were broken down. The cylindrical electrode is positioned around the flame area to generate plasma in the region. The flames were confined in the channel, on the one hand, to ensure the creation of a stable uniform plasma as a dielectric barrier, on the other hand, to isolate the influence of oxygen in the air on the combustion reaction. Further details regarding the experimental setup are reported in Ref. [8].

Fig. 1 showed the sampling position of the optical diagnostic system used to capture the detailed two-dimensional temperature distributions and *KL* factors (soot concentration information) in the flame. This work employed a two-color pyrometer to measure the two-dimensional distribution of temperature and *KL* factor due to the difficulties of direct contact temperature measurement of internal flame [29, 30]. The system consists of an optical probe, a charge-coupled device (CCD) camera with optical transmission, a frame grabber, a microcomputer, and associated software. The two-color pyrometer has been widely utilized to measure soot temperature and concentration in various combustion systems [8, 20, 31-34]. Based on the empirical

correlation in the references [35, 36], soot concentrations can be qualitatively compared by the *KL* factor. The higher the value of the *KL* factor, the higher the soot concentration. More detailed principles and derivation of the two-color pyrometer method were given in the previous study [8, 20, 37]. In this experiment, red (700 nm) and green (546 nm) wavelengths were selected as the temperature bands for measurement. In addition, for the flame instability existing with the plasma activation, at least four photographs were compared to determine the typicality and reproducibility of the results respectively.

Along the axis in the reaction chamber, a thermophoretic sampling was performed through a TEM grid mounted at the outlet of the quartz tube to study the morphology and nano-characteristics of soot particles. More than three locations were chosen during this process to assure the precision and reproducibility of the observations in TEM analysis. A new TEM copper grid was used for each sampling. This sampling system has also been used in previous work [27, 38, 39]. Additionally, more quantitative properties like fringe length and fringe tortuosity might be extracted from high resolution transmission electron microscopy (HRTEM) pictures [41] using a home-made Matlab program and the image processing technique suggested in the literature [40, 41].

Soot samples were harvested from a quartz plate located in the outlet of the reactor. This kind of sampling method has been successfully applied for soot analyses in various studies [8, 20, 27, 37-39]. The collection time here was 20 minutes to ensure sufficient material was obtained for subsequent characterization analysis. It has

been confirmed that the collection time does not significantly affect the soot characteristics [42]. X-ray diffraction (XRD) analysis was employed to determine the crystalline characteristics of soot particles produced by varied gas flow rates with plasma-flame interactions. An X-ray powder diffractometer (Rigaku D/max 2500 PC) with Cu-Kα X-ray source was employed. XRD patterns were obtained at 45 kV and 100 mA in the $2\theta$ range from 10° to 110° with a step size of $2\theta$ = 0.02° and an angular speed of 1 s/step. The oxidation reactivity of soot particles was assessed using a NETZSCH STA 449 F3 Jupiter thermogravimetric analyzer with recording software. In the thermogravimetric analysis experiment, three replications of the experiment under each condition were performed to establish the typicality and accuracy. Our earlier research showed that this method's accuracy was 95% with a 4.7% uncertainty [43].

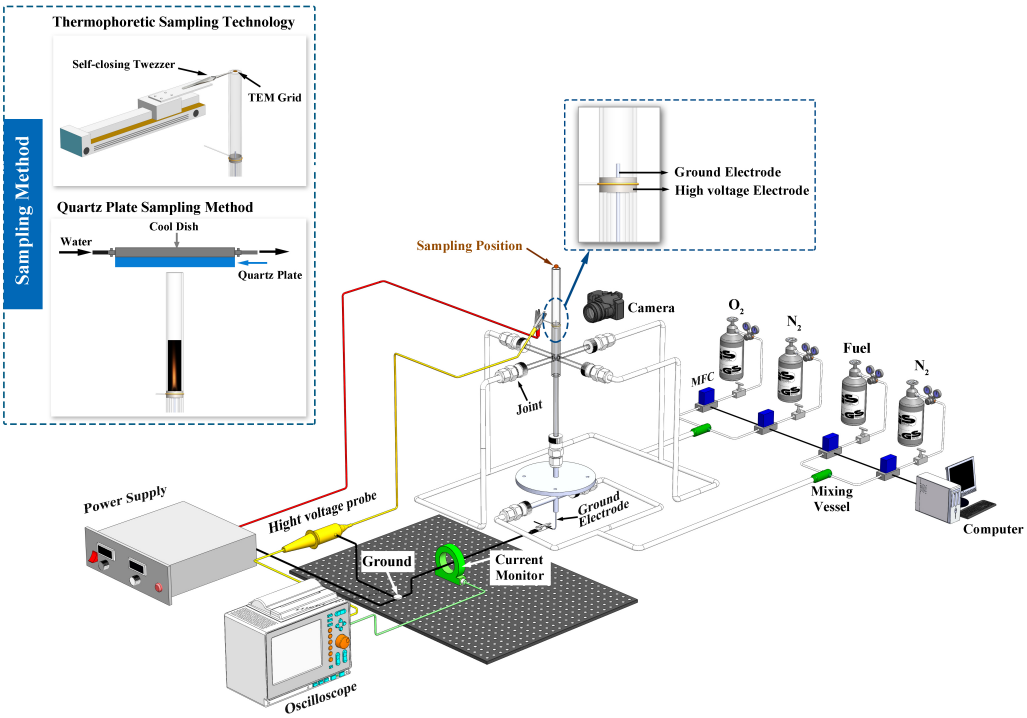


**Fig. 1.** Schematic diagram of experimental set up.

For the operating conditions, the reactants consisted of ethylene, nitrogen, and oxygen in a total of six cases corresponding to different carbon content as shown in Table 1. Since the flow rates in experiments differed only by the reactant flow rates at the same C/O ratio, a change in reactant flow rate was analogous to a change in carbon content. The summary of the electrical parameters and flow rates was displayed in Table 1. Table 1 lists several flame notations, including 125-0-0, 125-12-2.5, 150-0-0, 150-12-2.5, and 175-0-0 and 175-12-2.5.

**Table 1.** Flame experimental conditions.

| Flame notation | Applied voltage, $U$ (kV) | Discharge frequency, $f$ (kHz) | Carbon content ($mol_{carbon}/h$) | Gas flow rate (mL/min) | | | |
|---|---|---|---|---|---|---|---|
| | | | | $C_2H_4$ | $N_2$ (Diluent) | $O_2$ | $N_2$ (Carrier) |
| 125-0-0 | 0 | 0 | 0.612 | 125 | 83.3 | 189.6 | 352.1 |
| 125-12-2.5 | 12 | 2.5 | | | | | |
| 150-0-0 | 0 | 0 | 0.735 | 150 | 100 | 227.5 | 422.5 |
| 150-12-2.5 | 12 | 2.5 | | | | | |
| 175-0-0 | 0 | 0 | 0.857 | 175 | 116.7 | 265.5 | 492.5 |
| 175-12-2.5 | 12 | 2.5 | | | | | |

## 3. Results and discussion

### *3.1 Flame structure*

Fig. 2 provided the photographs of diffusion flames for all experimental conditions. The combustion process that occurred in the burner was non-premixed because the fuel and oxidizer were transported in separate channels before the flame formation. The diffusion flames stabilized at the internal tube outlet eventually, as shown in Fig. 1. Results demonstrated that with the increase of the gas flow rate, more gas can take part in combustion per time, which led to a higher flame height and larger combustion area, although the total C/O ratio was identical. With the increase of carbon content from 0.612 to 0.857 $mol_{carbon}/h$, the overall flame luminous intensity

increased significantly, due to inception, agglomeration, and escape of more soot particles [44]. The quantitative results of the flame temperatures and mass of formed soot would be given in section 3.2. Moreover, compared with the pure ethylene flame, the flame length for all the plasma-added flames was short and its radius was enlarged considerably, while the flame luminosity became lower. In this work, the distribution of plasma is still not absolutely uniform, which might cause the flame highly asymmetric when the plasma was applied. This was consistent with the results of our previous experiments [8, 9]. Kim et al. [45] suggested that the flame length was generally determined by the balance of axial convection and radial diffusion. The radial caused by ionic winds convection might reduce the flame length in strong streamers [9, 46, 47]. Due to the heavy dependence of polycyclic aromatic hydrocarbons (PAHs) and soot formation on temperature, residence time, and fuel mole fraction [48], the modified flow field via the ionic wind may produce an unfavorable environment for soot formation and growth.

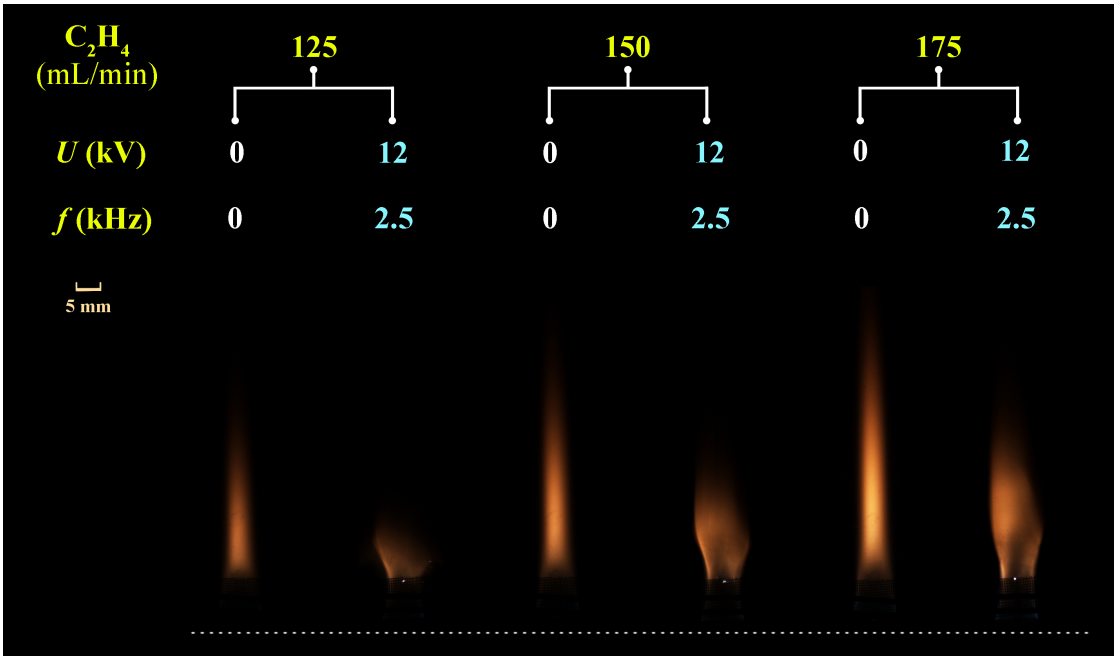

**Fig. 2.** Representative images of flames under the same excess C/O ratio at various conditions.

*3.2 Optical combustion characteristics*

Six different experimental conditions were selected to show the evolution of soot temperature and *KL* factor distributions with three gas flow rates for plasma-flame interaction. The spatial distributions of soot temperature and *KL* factors under various conditions were depicted in Fig. 3. The temperature and *KL* factor photos in this section mostly depict the soot area. It should be mentioned that all the cases adopt the same optical parameters to obtain comparable flame characteristics and statistical results. The images were calculated from two-color pyrometry at wavelengths of 700 nm and 546 nm.

According to Fig. 3(a), under the without-plasma condition (125-0-0, 150-0-0, and 175-0-0), the mean temperature ($T_{mean}$) remained constant approximately. It could be explained that the total C/O ratio remained constant, which meant that the amount of oxidizer supplied to the same amount of fuel per unit time was consistent. When the plasma interacted with the flame (125-12-2.5, 150-12-2.5, 175-12-2.5), the average temperature tended to rise slightly compared to without plasma. As exhibited in Fig.3(a), the low-temperature region in the flame downstream after adding plasma was reduced. The distribution of high-temperature regions was more concentrated, and the local temperature was higher.

The *KL* factor could be used to qualitatively compare the soot concentration, with larger values indicating higher soot concentrations in the region [49]. The mean *KL* factor ($KL_{mean}$) was marked above each image, respectively. In Fig. 3(b), without

the presence of plasma, $KL_{mean}$ grew dramatically as gas flow rates increased, because of a growing number of carbons participating in the combustion process. As shown in Fig. 3(b), the soot concentration decreased rapidly with plasma generation. This tendency was in accordance with the findings of Park et al. [50] and the visual observation of flame luminosity in Fig. 2 from the preceding section. The soot concentration might be affected by several factors simultaneously under the plasma-flame interaction. Manyo et al demonstrated that soot growth was more or less associated with charged species and it can be controlled by an electric field [51]. Plasma-induced reaction intensification may aid the reduction of ionic species into non-soot precursors, hence the lowering formation of soot precursors [52]. The enhanced interaction between the electrons and the gas led to the creation of more active species, which might aid in the oxidation of the soot. Moreover, changes in flame length affect the residence time of soot growth, which in turn affects the soot concentration in the flame. In the case of the same gas flow rate, the residence time during the soot emissions was decreased in the combustion with the plasma addition.

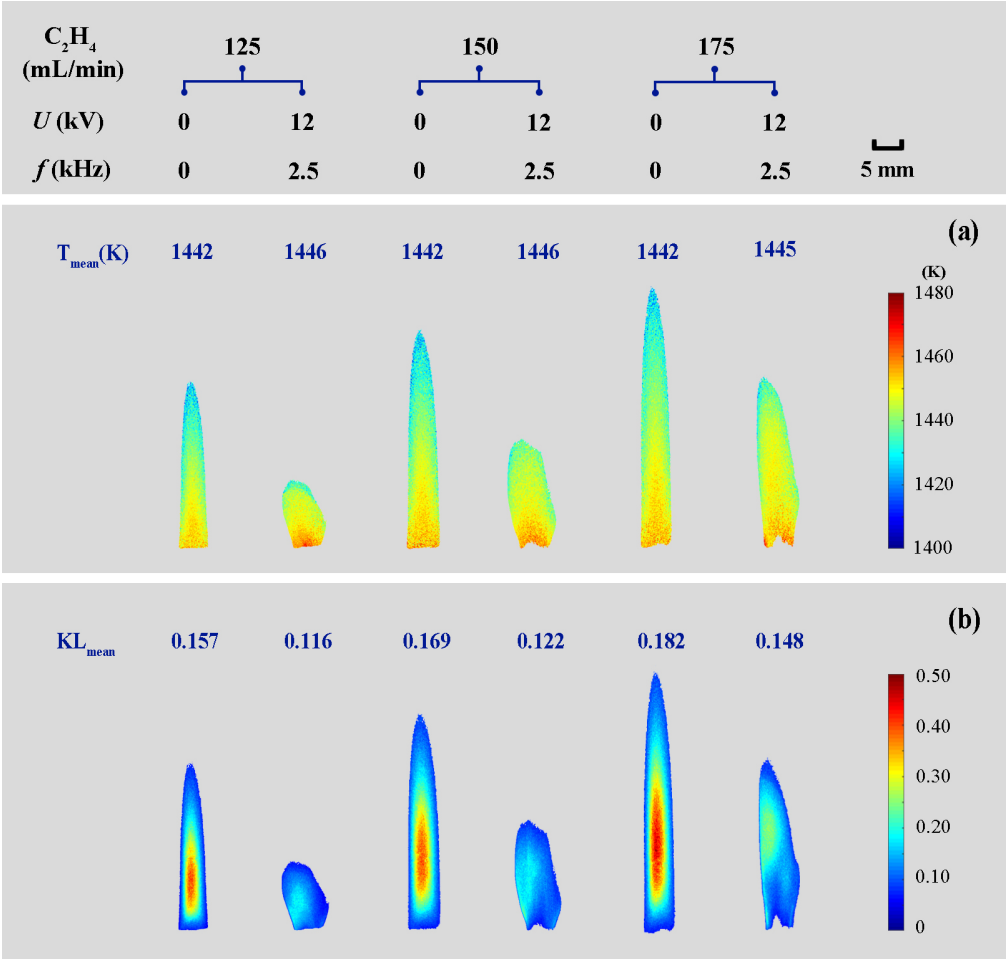


**Fig. 3.** Temperature (a) and *KL* factor (b) distributions with the variation of discharge conditions in the combustor.

*3.3 Soot morphology and nanostructure*

Differences in soot morphology and nanostructure contribute to an improved understanding of soot formation characteristics. Particles collected on a TEM grid via thermophoretic sampling were shown in Fig. 4. As mentioned in the Section 2, it could be observed that the soot morphology characteristic altered with the increase of gas flow rates. Most of the primary particles were very similar in size (Fig. 4a-c). Although soot particles produced by increased carbon content were similar in size, it was difficult to directly assess the oxidation activity of this part of soot. The soot

generated in pure flames (Figs. 4a, b, and c) showed that the dispersed irregularly shaped protrusions were formed and covered by some liquid-like material with the increase of gas flow rates. It should be noted that soot from 125-12-2.5 presented as liquid-like material with irregularly shaped protrusions (Fig. 4(d)). The soot was transparent and sticky. The film-like deposition was in an irregular shape and it was difficult to distinguish individual particles. This structure evolved from the chemical condensation of heavy polycyclic aromatic hydrocarbons, which suggests that soot is still young [53]. At the higher gas flow rates (150-12-2.5 and 175-12-2.5), chain-like aggregates were formed but still covered with liquid material, as illustrated in Fig.4(e) and (f). With the flow rate increased, the soot in Figs. 4(e) and f showed a lower amount of the liquid-like material than the soot in Fig. 4(a). The observations were similar to those reported in the literature [30, 53].

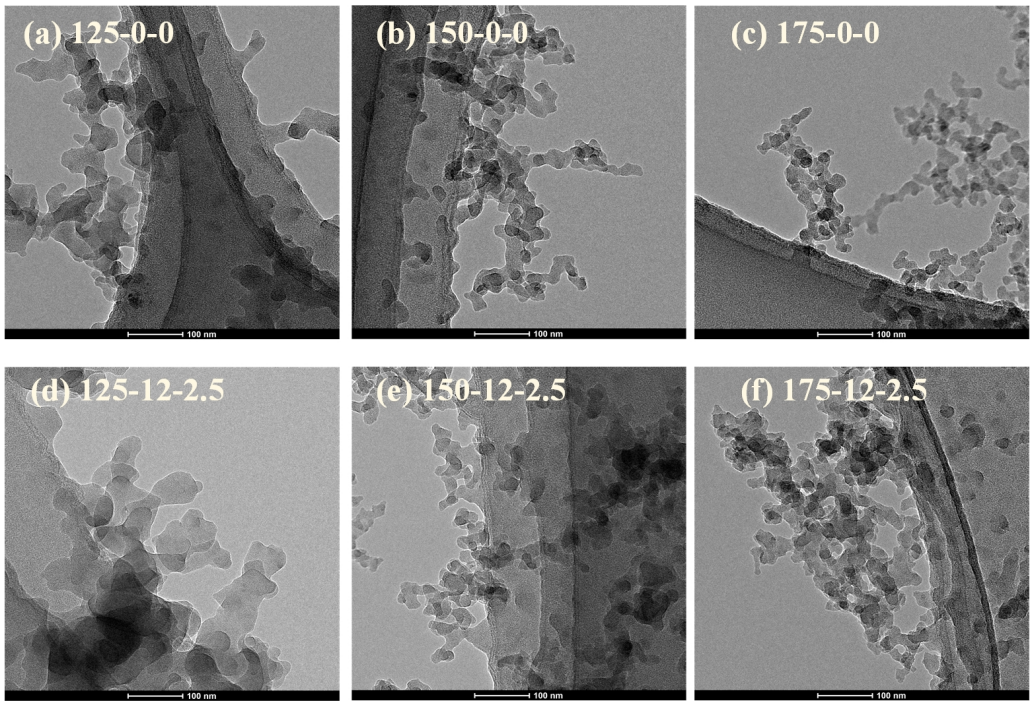


**Fig. 4.** Morphology transition of soot (length scale of 100 nm, with 75,000× magnification) with various plasma discharge conditions.

For quantitative information, several TEM images of soot generated from pure flames and plasma-flame interactions were processed using Nano Measurer software to evaluate the average sizes of primary particles. Fig. 5 depicted the mean primary particle diameter ($d_p$) of soot particles from flames with various plasma discharge conditions. $d_p$ decreased due to the soot oxidation with the gas flow rate ranging from 125 to 175 mL/min. As the discharge frequency increased, a larger $d_p$ could be obtained. In fact, on the one hand, it might be because the particles are bigger and more nascent containing film-like particles. On the other hand, the flame with plasma discharge was distinctly shorter than without plasma, which reduced the oxidation process in combustion. Thus, the degree of soot oxidation with plasma activation was reduced, which resulted in a larger particle size.

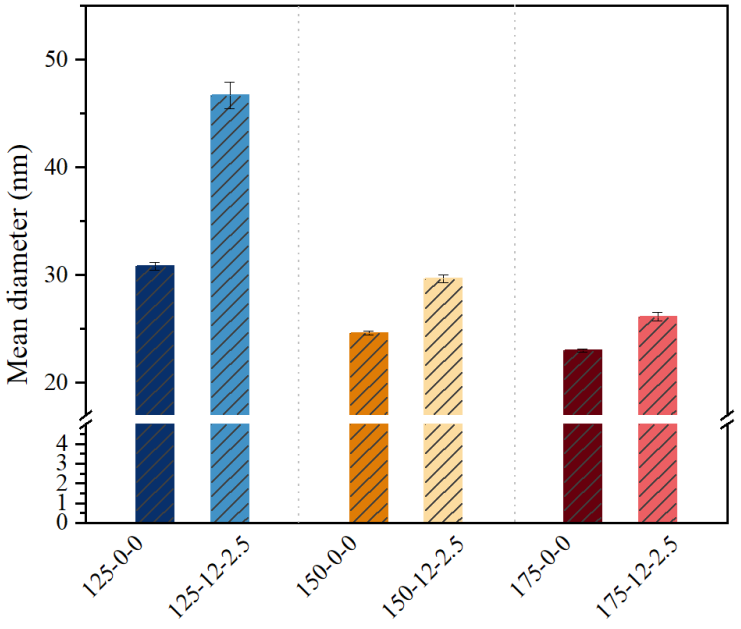


**Fig. 5.** Mean diameter of soot particles

Fig. 6 exhibited the HRTEM images and corresponding extracted skeleton images for different flow rates in all conditions. The parallel fringes reflected the

existence of graphitization segments, while the curved fringes represented a large number of PAHs [54]. As indicated in Fig. 6(a-c), the soot carbonization degree increased with the increase of gas flow rates because the longer residence time was simultaneously obtained, which was beneficial to the formation of soot with higher maturity. The soot particles from pure flame all appeared the typical fullerene-like structure composed of much-curved lamellae with small diameters, suggesting the simultaneous existence of graphitic parts and PAHs, while the soot from the interaction of flame and plasma seemed that more amorphous structures emerged.

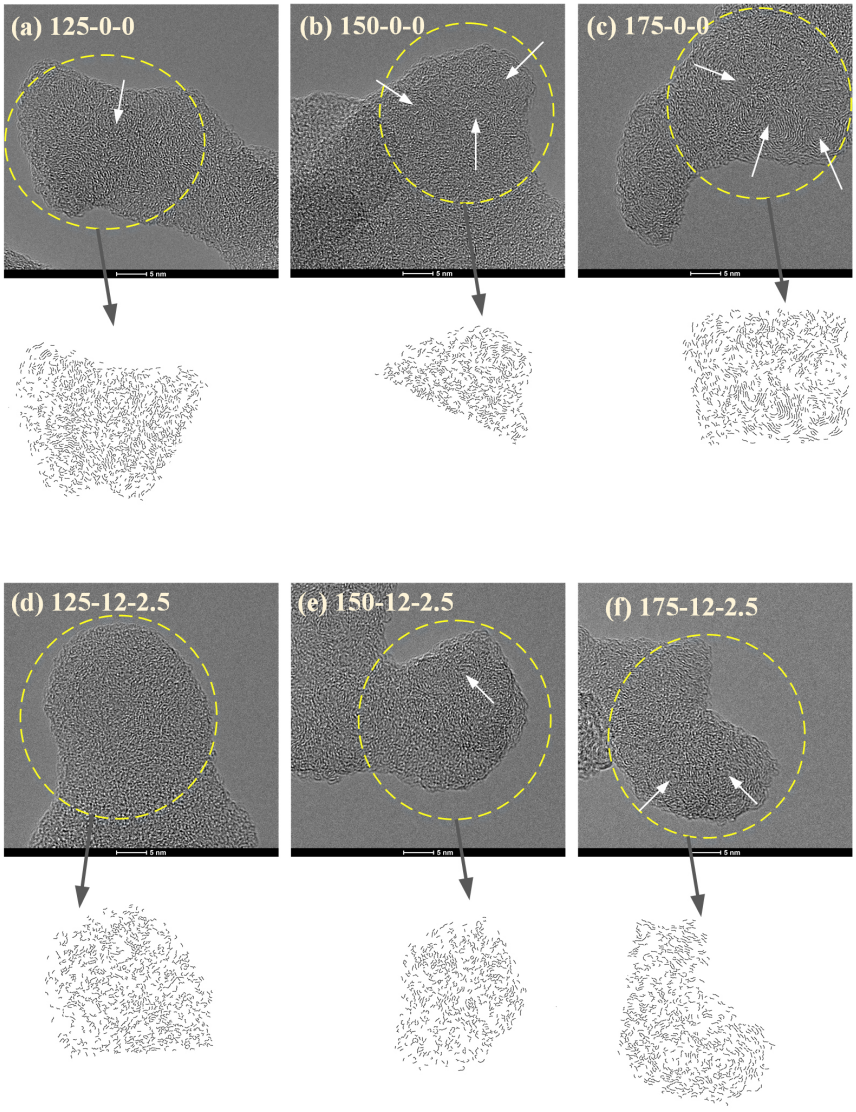

**Fig. 6.** Representative HRTEM (with 1,000,000× magnification) and the corresponding extracted skeleton images of soot for the variation of flow rate with (d-f) and without (a-c) the plasma-flame interaction.

Soot fringe length and tortuosity were retrieved from skeletal pictures for comprehensive quantitative studies. Fig. 7 depicted the lognormal curve fitting of the fringe length and tortuosity distributions. It could be found that the mean fringe length increased and the fringe tortuosity decreased slightly with the carbon content increased. The mean fringe length showed a sequence as 125-12-2.5 (0.74±0.01 nm) < 150-12-2.5 (0.77±0.01 nm) < 175-12-2.5 (0.78±0.01 nm) < 125-0-0 (0.81±0.01 nm) < 150-0-0 (0.82±0.01 nm) < 175-0-0 (0.88±0.02 nm). In Fig. 7(b), the rankings of mean value of fringe tortuosity for the variation of experimental conditions corresponded to 125-12-2.5 (1.37 ± 0.03 nm) > 150-12-2.5 (1.31 ± 0.02 nm) > 175-12-2.5 (1.29±0.02 nm) > 125-0-0 (1.26±0.02 nm) > 150-0-0 (1.23±0.03 nm) > 175-0-0 (1.21±0.01 nm). As the carbon content increased, the fringe length increased but the fringe tortuosity slightly reduced. The elongation in fringe length and reduction in fringe tortuosity demonstrated that with increasing carbon content supply, the generated soot has a higher degree of carbonization [12, 13, 42]. Moreover, more tortuous and shorter fringes were observed in the nanostructure of soot particles at the plasma-flame interactions than that from pure flames, which was consistent with the visual comparison of HRTEM images. The decrease in lamella length could be attributed to the more active substances in plasma-flame interactions, which was adverse to the soot formation and growth. On the other hand, the flame with plasma

discharge was distinctly shorter than without plasma, which reduced the oxidation process in combustion. These data indicated that the lower carbonization degree of soot was formed with the plasma activated in flame, which was similar to the previous TEM analysis in that the soot formation was suppressed with plasma addition.

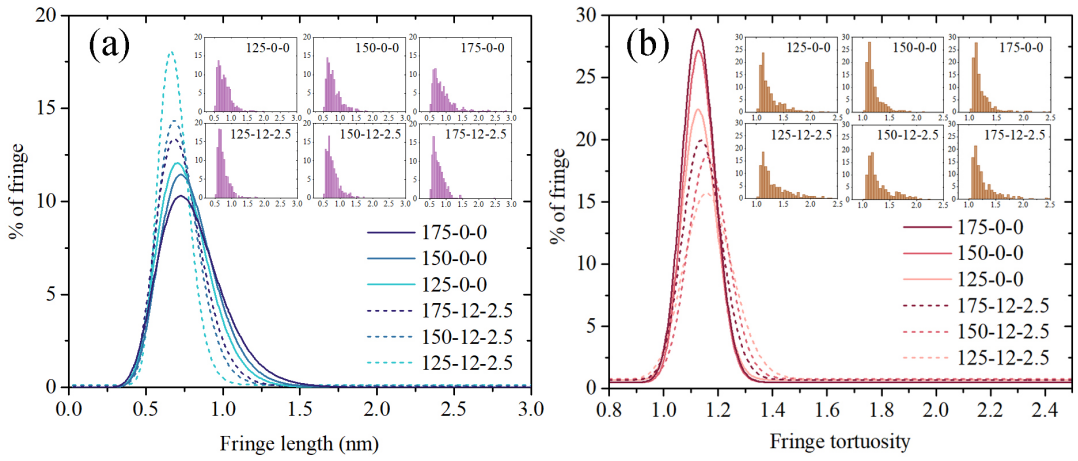


**Fig. 7.** (a) Fringe length, (b) fringe tortuosity profiles of soot in lognormal curve fittings with different conditions. Insets: histograms of fringe length and tortuosity for different conditions.

*3.4 XRD analysis of Soot particles*

Fig. 8 provided the baseline corrected diffraction patterns of soot at different gas flow rates with or without plasma addition. In Fig. 8, the 125-12-2.5 curve was deficient due to the relatively low soot yield at this condition, making it difficult to peel soot from the plate and complete the XRD test. The peak around $2\theta$ = 24° is assigned to the (002) plane [55]. The peak around $2\theta$ = 24° is broad, indicating insufficient soot graphitization in the nanostructure, which leads to a significant amorphous feature and a low degree of structural order. The XRD data could be used to analyze quantitative information about the soot crystalline structure and its fluctuations with different conditions. The soot diffraction peak shifted to the right for

the conditions of increasing gas flow rates (125-0-0, 150-0-0, and 175-0-0), as shown by the differences in diffraction angles mentioned in Fig. 9, suggesting that the increase of gas flow rate caused the greater soot graphitization degree. The soot peak always migrated to the right for the plasma-flame interaction circumstances (150-12-2.5 and 175-12-2.5). Additionally, in the case of the same carbon content, the peak diffraction angles reduced with the plasma-flame interaction, which showed the decline in soot graphitization degree.

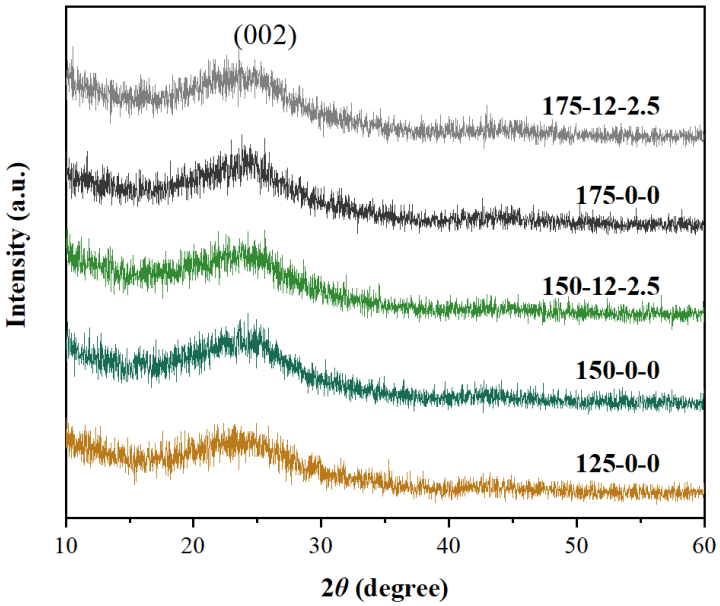


**Fig. 8.** X-ray diffraction (XRD) patterns of soot particles under different flame conditions.

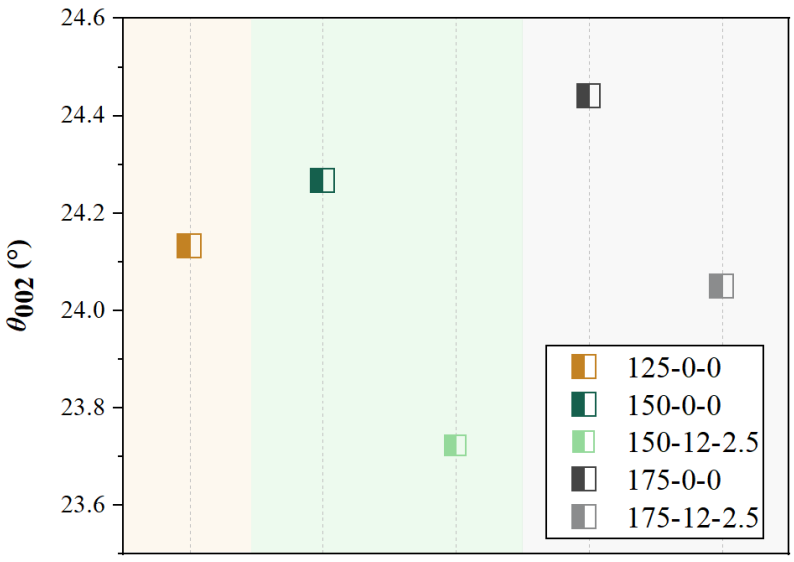

**Fig. 9.** The peak diffraction angles of soot particles under different conditions.

*3.5 Isothermal oxidation of soot*

The normalized mass loss curves of the soot sample during the isothermal oxidation process were shown in Fig. 10. Due to the extremely low soot product at 125-12-2.5 condition, it was very difficult to peel off soot from the quartz plate, which was why the 125-12-2.5 mass loss curve was missing from Fig. 10. The total mass loss curves showed a similar trend but different oxidation rates [56]. A higher soot oxidation rate (mass loss curve slope) indicated higher reactivity, which implied that the soot was simpler to oxidize. In Fig. 10, the slopes of normalized mass loss curves ranked as 175-0-0 < 150-0-0 < 125-0-0 and 175-12-2.5 < 150-12-2.5, which suggested that the soot oxidation reactivity decreased as the gas flow rates increased. This trend was the same for soot from the diffusion flames with and without plasma. In addition, the slopes of the normalized mass loss curves rose in the following sequence with the same flow rate: 150-0-0 < 150-12-2.5 and 175-0-0 < 175-12-2.5. It demonstrated that the oxidation reactivity of soot decreased all the time with the plasma addition at the same gas flow rates. This phenomenon was similar to the flow-induced difference of TEM images observed in Fig. 4. Furthermore, the slopes of the normalized mass loss curves of soot from the pure flame were consistently substantially lower than those from the plasma-flame interaction, indicating that the soot with plasma addition had the higher oxidation reactivity. The TGA results further confirmed the distinct different soot properties caused by the plasma activation.

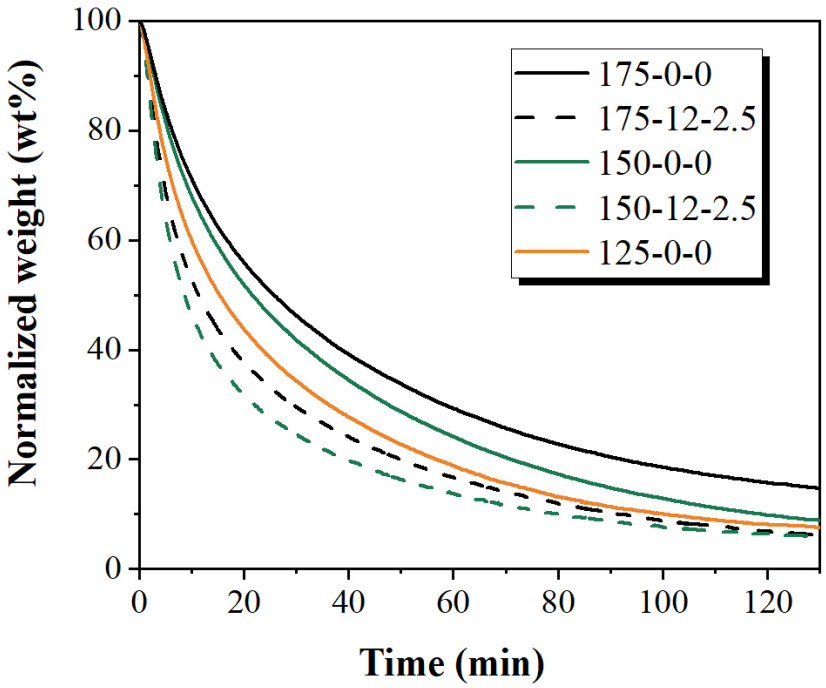


**Fig. 10.** TGA curves of soot particles for the various discharge conditions.

## 4. Conclusion

Understanding the evolution of soot particle morphology and reactivity in plasma-flame interaction is of interest for enabling targeted control of soot emissions in combustion. One of the major questions was to study a certain parameter (or set of parameters) drove the evolution of soot characteristics in the plasma-flame interaction. To elucidate on this matter, this study examined how the gas flow rate affected the morphology and characteristic of soot particles in the plasma-flames interactions. To do so, we have characterized the two-dimensional temperature and soot concentration distributions via a two-color pyrometer. Moreover, we have determined the morphology, nanostructure, and oxidation reactivity of soot particles at different gas flow rates using ex-situ techniques (HRTEM, XRD, and TGA).

This work has confirmed that the gas flow rate variation and the plasma addition affected the flame shapes and luminosity. Results demonstrated that with the increase

of the carbon, more gas can take part in combustion per time, which led to a higher flame height and larger combustion area as well as greater flame overall luminous. The flame length was decreased as the plasma was coupled to the flame, which might be attributed to the increase of radial convection induced by ionic wind. There was an evident increase in the temperature and soot concentration when the gas flow rate increased. The overall soot concentration decreased rapidly with plasma generation at the same flow rate. The residence time of soot growth is affected by variations in flame length, which in turn influences the soot concentration in the flame. Plasma-induced reaction intensification could assist the conversion of ionic species into non-soot precursors, decreasing soot precursor emissions. TEM results showed that the soot particles from the plasma-flame interaction had somewhat bigger diameters than the pure ethylene soot without plasma by visual comparison. Soot nanostructure and reactivity were shown to have strong connections. The particles from plasma-activated flames had shorter fringe lengths and larger fringe tortuosity related to higher oxidation reactivity. However, the higher carbon content caused a higher degree of carbonization in the soot nanostructure and then reduced the soot oxidation rate.

**Acknowledgments**

This work was supported by the National Natural Science Foundation of China [52076110, 52376115].

**References**


[1] Han Y, An Z, Arimoto R, et al. Sediment soot radiocarbon Indicates that recent prollution controls slowed fossil fuel emissions in southeastern China. Environ Sci Technol, 2022, 56: 1534–1543.

[2] Lin Y, Huang X, Liu Y, et al. Identification, quantification, and imaging of the biodistribution of soot particles by mass spectral fingerprinting. Anal Chem, 2021, 93: 6665–6672.

[3] Shi J, Qi H, Yu Z, An X, Ren Y, Tan H. Three-dimensional temperature reconstruction of diffusion flame from the light-field convolution imaging by the focused plenoptic camera. Sci China Technol Sci, 2022, 65: 302–323.

[4] Reich B J, Fuentes M, Burke J. Analysis of the effects of ultrafine particulate matter while accounting for human exposure. Environmetrics, 2009, 20: 131–146.

[5] Huang S, Wu Y, Zhang K, et al. Experimental investigation of spray characteristics of gliding arc plasma airblast fuel injector. Fuel, 2021, 293: 120382.

[6] De Giorgi M G, Ficarella A, Sciolti A, et al. Improvement of lean flame stability of inverse methane/air diffusion flame by using coaxial dielectric plasma discharge actuators. Energy, 2017, 126: 689–706.

[7] Siva Nagaraju A, Verma K A, Pandey K M, et al. Numerical analysis of plasma combustion in scramjet engine-A review. Mater Today Proc, 2020, 45: 6838–6851.

[8] Qi D, Ying Y, Mei D, et al. Soot characteristics from diffusion flames coupled with plasma. Fuel, 2023, 332: 126126.

[9] Cha M S, Lee S M, Kim K T, et al. Soot suppression by nonthermal plasma in coflow jet diffusion flames using a dielectric barrier discharge. Combust Flame, 2005, 141: 438–447.

[10] Choe J, Sun W, Ombrello T, et al. Plasma assisted ammonia combustion: Simultaneous $NO_x$ reduction and flame enhancement. Combust Flame, 2021, 228: 430–432.

[11] Ashford B, Tu X. Non-thermal plasma technology for the conversion of $CO_2$. Curr Opin Green Sustain Chem, 2017, 3: 45–49.

[12] Taneja T S, Johnson P N, Yang S. Nanosecond pulsed plasma assisted combustion of ammonia-air mixtures: Effects on ignition delays and $NO_x$ emission. Combust Flame, 2022, 245: 112327.

[13] Han J, Yamashita H. Numerical study of the effects of non-equilibrium plasma on the ignition delay of a methane-air mixture using detailed ion chemical kinetics. Combust Flame, 2014, 161: 2064–2072.

[14] Patel R, Van Oijen J, Dam N, et al. Low-temperature filamentary plasma for ignition-stabilized combustion. Combust Flame, 2023, 47: 112501.

[15] Barleon N, Cheng L, Cuenot B, et al. Investigation of the impact of NRP discharge frequency on the ignition of a lean methane-air mixture using fully coupled plasma-combustion numerical simulations. Proc Combust Inst, 2022, 000: 1–10.

[16] Lin Q, Jiang Y, Liu C, et al. Controllable NO emission and high flame performance of ammonia combustion assisted by non-equilibrium plasma. Fuel, 2022, 319: 123818.

[17] Ban Y, Zhong S, Zhu J, et al. Effects of non-equilibrium plasma and equilibrium discharge on low-temperature combustion in lean propane/air mixtures. Fuel, 2023, 339: 127353.

[18] Ju Y, Sun W. Plasma assisted combustion: Dynamics and chemistry. Prog Energy Combust Sci, 2015, 48: 21–83.

[19] Varella R A, Sagás J C, Martins C A. Effects of plasma assisted combustion on pollutant emissions of a premixed flame of natural gas and air. Fuel, 2016, 184: 269–276.

[20] Qi D, Yang K, Zhao X, et al. Comprehensive optical diagnostics for flame behavior and soot emission response to a non-equilibrium plasma. Energy, 2022, 255: 124555.

[21] Tamadonfar P, Gülder Ö L. Effect of burner diameter on the burning velocity of premixed turbulent flames stabilized on Bunsen-type burners. Exp Therm Fluid Sci, 2016, 73: 42–48.

[22] Shi Y, Lu Y, Cai Y, et al. Evolution of particulate matter deposited in the DPF channel during low-temperature regeneration by non-thermal plasma. Fuel, 2022, 318: 123552.

[23] Okubo M, Yamada H, Yoshida K, et al. Simultaneous reduction of diesel particulate and $NO_x$ using a catalysis-combined nonthermal plasma reactor.

IEEE Trans Ind Appl, 2017, 53(6): 5875–5882

[24] Fortugno P, Musikhin S, Shi X, et al. Synthesis of freestanding few-layer graphene in microwave plasma: The role of oxygen. Carbon, 2022, 186: 560–573.

[25] López-Cámara C-F, Fortugno P, Asif M, et al. Evolution of particle size and morphology in plasma synthesis of few-layer graphene and soot. Combust Flame, 2023: 112713.

[26] Martínez-Aguilar J, González-Gago C, Castaños-Martínez E, et al. Influence of gas flow on the axial distribution of densities, temperatures and thermodynamic equilibrium degree in surface-wave plasmas sustained at atmospheric pressure. Spectrochim Acta-Part B At Spectrosc, 2019, 158: 105636.

[27] Chen M, Liu D, Ying Y, et al. Experimental study on soot formation, evolution and characteristics of diffusion ethylene/air flames in Ψ-shaped mesoscale combustors. Fuel, 2019, 241: 138–154.

[28] Dubey AK, Tezuka T, Hasegawa S. Study on sooting behavior of premixed C1–C4 n-alkanes/air flames using a micro flow reactor with a controlled temperature profile. Combust Flame, 2016, 174: 100–110.

[29] Liu H, Huang J, Li L, et al. Volumetric imaging of flame refractive index, density, and temperature using background-oriented Schlieren tomography. Sci China Technol Sci, 2021, 64: 98–110.

[30] Wang Q, Liu H, Cai W, et al. Development of a single-camera volumetric

thermometry for gas flows based on space division multiplexing. Sci China Technol Sci, 2022, 65: 1646–1650.

[31] Li L, Duan L, Yang Z, et al. Pressurized oxy-fuel combustion characteristics of single coal particle in a visualized fluidized bed combustor. Combust Flame, 2020, 211: 218–228.

[32] Karataş AE, Gülder Ö L. Dependence of sooting characteristics and temperature field of co-flow laminar pure and nitrogen-diluted ethylene-air diffusion flames on pressure. Combust Flame, 2015, 162: 1566–1574.

[33] Abhinavam Kailasanathan R K, Yelverton T L B, Fang T, et al. Effect of diluents on soot precursor formation and temperature in ethylene laminar diffusion flames. Combust Flame, 2013, 160: 656–670.

[34] Shui C, Liu H, Cai W. Benchmark evaluation of tomographic algorithms for simultaneous reconstruction of temperature and volume fraction fields of soot and metal-oxide nanoparticles in non-uniform flames. Sci China Technol Sci, 2021, 64: 237–250.

[35] Zhang J, Jing W, Roberts WL, et al. Soot temperature and *KL* factor for biodiesel and diesel spray combustion in a constant volume combustion chamber. Appl Energy, 2013, 107: 52–65.

[36] Chen H, Su X, He J, et al. Investigation on combustion characteristics of cyclopentanol/diesel fuel blends in an optical engine. Renew. Energy, 2021, 167: 811–829.

[37] Chen M, Liu D. Morphology and nanostructure transitions of soot with various

dimethyl ether additions in nonpremixed ethylene flames at different scales. Energy Fuels, 2020, 34(12): 16705–16719.

[38] Duan J, Ying Y, Liu D. Novel nanoscale control on soot formation by local $CO_2$ micro-injection in ethylene inverse diffusion flames. Energy, 2019, 179: 697–708.

[39] Ying Y, Liu D. Nanostructure evolution and reactivity of nascent soot from inverse diffusion flames in $CO_2$, $N_2$, and He atmospheres. Carbon, 2018, 139: 172–180.

[40] Vander Wal R L, Tomasek A J, Pamphlet M I, et al. Analysis of HRTEM images for carbon nanostructure quantification. J Nanoparticle Res, 2004, 6: 555–568.

[41] Yehliu K, Vander Wal R L, Boehman A L. Development of an HRTEM image analysis method to quantify carbon nanostructure. Combust Flame, 2011, 158: 1837–1851.

[42] Ying Y, Liu D. Effects of butanol isomers additions on soot nanostructure and reactivity in normal and inverse ethylene diffusion flames. Fuel, 2017, 205: 109–129.

[43] Ying Y, Xu C, Liu D, et al. Nanostructure and oxidation reactivity of nascent soot particles in ethylene/pentanol flames. Energies, 2017, 10: 4–6.

[44] Lu W, Mao Q, Chu F M, et al. Experimental and simulation studies on flame characteristics and soot formation of $C_2H_2$ jet flames. Fuel, 2023, 343: 127814.

[45] Kim S, Han K, Baek S. Influence of DC Electric Field on the Propane-Air

Diffusion Flames and $NO_x$ Formation. Energies, 2021, 14: 1–12.

[46] Lacoste D A. Flames with plasmas. Proc Combust Inst, 2022, 000: 1–24.

[47] Ghabi A, Darny T, Dozias S, et al. Effects of pulsed gliding arc plasma on non-premixed $CH_4/CO_2$– air flame stability. Therm Sci Eng Prog, 2023, 40: 101764.

[48] Joo P H, Wang Y, Raj A, et al. Sooting limit in counterflow diffusion flames of ethylene/propane fuels and implication to threshold soot index. Proc Combust Inst, 2013, 34(1): 1803–1809.

[49] Yi W, Liu H, Feng L, et al. Multiple optical diagnostics on effects of fuel properties on spray flames under oxygen-enriched conditions. Fuel, 2021, 291: 120129.

[50] Park D G, Choi B C, Cha M S, et al. Soot reduction under DC electric fields in counterflow non-premixed laminar ethylene flames. Combust Sci Technol, 2014, 186(4-5): 644–656.

[51] Manyo P, Weinberg F. On the size, charge and number-rate of formation of carbon particles in flames subjected to electric fields. Proc R Soc Lond A Math Phys Sci, 1970, 319: 351–371.

[52] Matsuzawa Y, Suzuki J, Horisawa H, et al. Effect of electron injection for soot suppression in hydrocarbon flames. Vacuum, 2013, 88: 79–82.

[53] Chen M, Liu D, Jiang B. Soot formation and combustion characteristics in confined mesoscale combustors under conventional and oxy-combustion conditions ($O_2/N_2$ and $O_2/CO_2$). Fuel, 2020, 264: 116808.

[54] Xiao H, Hou B, Zeng P, et al. Combustion and emission characteristics of diesel engine fueled with 2,5-dimethylfuran and diesel blends. Fuel, 2017, 192: 53–59.

[55] Frusteri L, Cannilla C, Barbera K, et al. Carbon growth evidences as a result of benzene pyrolysis. Carbon, 2013, 59: 296–307.

[56] Zhang L, Liu D. Formation and characteristics of soot from pyrolysis of ethylene blended with furan fuels. Sci China Technol Sci, 2021, 64: 585–598.